OUKA
The University of Osaka
Institutional Knowledge Archive

Title	Neural network potential for dislocation plasticity in ceramics
Author(s)	Zhang, Shihao; Li, Yan; Suzuki, Shuntaro et al.
Citation	npj Computational Materials. 2024, 10, p. 266
Version Type	VoR
URL	https://hdl.handle.net/11094/100441
rights	This article is licensed under a Creative Commons Attribution 4.0 International License.
Note	

The University of Osaka Institutional Knowledge Archive : OUKA

https://ir.library.osaka-u.ac.jp/

The University of Osaka

npj | computational materials

Article

Published in partnership with the Shanghai Institute of Ceramics of the Chinese Academy of Sciences

https://doi.org/10.1038/s41524-024-01456-7

Neural network potential for dislocation plasticity in ceramics

Check for updates

Shihao Zhang [1], Yan Li [1], Shuntaro Suzuki[2], Atsutomo Nakamura[1] & Shigenobu Ogata [1]

Dislocations in ceramics are increasingly recognized for their promising potential in applications such as toughening intrinsically brittle ceramics and tailoring functional properties. However, the atomistic simulation of dislocation plasticity in ceramics remains challenging due to the complex interatomic interactions characteristic of ceramics, which include a mix of ionic and covalent bonds, and highly distorted and extensive dislocation core structures within complex crystal structures. These complexities exceed the capabilities of empirical interatomic potentials. Therefore, constructing neural network potentials (NNPs) emerges as the optimal solution. Yet, creating a training dataset that includes dislocation structures proves difficult due to the complexity of their core configurations in ceramics and the computational demands of density functional theory for large atomic models containing dislocation cores. In this work, we propose a training dataset from properties that are easier to compute via high-throughput calculation. Using this dataset, we have successfully developed NNPs for dislocation plasticity in ceramics, specifically for three typical functional ceramics: ZnO, GaN, and $SrTiO_3$. These NNPs effectively capture the nonstoichiometric and charged core structures and slip barriers of dislocations, as well as the long-range electrostatic interactions between charged dislocations. The effectiveness of this dataset was further validated by measuring the similarity and uncertainty across snapshots derived from large-scale simulations, alongside extensive validation across various properties. Utilizing the constructed NNPs, we examined dislocation plasticity in ceramics through nanopillar compression and nanoindentation, which demonstrated excellent agreement with experimental observations. This study provides an effective framework for constructing NNPs that enable the detailed atomistic modeling of dislocation plasticity, opening new avenues for exploring the plastic behavior of ceramics.

Dislocations in both structural and functional ceramics are rapidly gaining attention due to their intriguing potential in property tuning, and thus are now perceived as promising atomic-scale entities for next-generation device applications[1–10]. As a type of topological one-dimensional defect, dislocations in ceramics feature non-stoichiometry and excess charge at their cores and local strain field around the cores, making them powerful entities for "defect engineering". By manipulating dislocations into ceramics or interacting dislocations with other defects, one can harness unprecedented mechanical properties and tailored functional properties. Examples include exceptional plasticity[6], anisotropic thermal transport[7], controllable ferroelectric properties[8,9], and enhanced photoconductivity[10]. Despite the significant effect and exciting application potential of dislocations in ceramics, the detailed structure and stability of dislocations, as well as the atomic-scale understanding of dislocation behaviors, are still challenging mainly due to their complication of the basic crystalline structures and the technical difficulty of the experiment, e.g., well-prepared samples and high-resolution ultramicroscopy[11,12].

Atomistic simulations play increasingly important roles in revealing atomic-scale insights into dislocations in ceramics. Density functional theory (DFT) calculations provide detailed atomic and electronic structures but are limited by the size and time scales it can handle. This restricts its use for many dislocation-related problems in ceramics, e.g., dislocation interaction with grain boundary[13], which often needs models with thousands to millions of atoms. In contrast, molecular dynamics (MD) simulations can study large systems of millions of atoms on a nanosecond scale. The challenge in conducting realistic MD simulations lies in the requirement for a

[1]Department of Mechanical Science and Bioengineering, Graduate School of Engineering Science, Osaka University, Osaka, 560-8531, Japan. [2]Union Tool Co. Ltd., Tokyo, 140-0013, Japan. e-mail: ogata.shigenobu.es@osaka-u.ac.jp

natural interatomic potential. A wide array of empirical and semi-empirical potentials have been developed for ceramics, including the rigid ion model[14], Stillinger-Weber (SW)[15], Vashishta[16], ReaxFF[17], COMB3[18], and SMTB-Q[19] potentials. However, many of these potentials were not designed to describe dislocations. The verification of their predictive power has been limited to relatively narrow domains of physical conditions directly relevant to their applications in the initial studies. These empirical potentials, based on fixed analytical function forms, lack the sophistication to accurately capture the energy surface of highly distorted dislocation core structures.

In recent years, advances in integrating DFT calculations with machine learning have led to the development of neural network potentials (NNPs)[20], which learn the potential energy landscape directly from reference DFT datasets[21]. They maintain near-DFT accuracy while affording atomic resolution at larger system sizes and time scales, comparable to classical interatomic potentials. NNPs have been successfully developed for several ceramic materials, e.g., TiO_2[22], ZnO[23], TiN[24], Cu_2O[25], $KNbO_3$[26], GaN[27], $SrTiO_3$[28], and HfO_2[29]. Most of these potentials focus on near-equilibrium configurations, with few being validated for modeling and simulating dislocations. Several NNPs have been constructed and validated for dislocations in metals and their alloys[30–33]. However, given the significant differences between dislocation nature in metals and ceramics, such as the nonstoichiometric and charged dislocation core in ceramics[34] and the mixed ionic-covalent bonding in ceramic materials, developing NNPs for dislocation plasticity in ceramics remains particularly challenging.

The primary issue lies in generating a training dataset that includes dislocation structures due to the complexity of their core configurations in ceramics and the computational demands involved, typically requiring the models composed of hundreds of atoms. This issue has also impeded the construction of NNPs for dislocation plasticity in ceramics using the newly developed on-the-fly active learning technology[35,36]. Active learning employs biased or unbiased MD simulation to generate candidate pools serving as training datasets. Active learning automatically targets regions with inaccurate energy predictions, eliminating the manual trial-and-error process of evaluating potential performance and designing new training configurations. Capturing the highly distorted dislocation core structures within this framework is particularly difficult because these structures exist in high-energy states, making them rare events[37]. As a result, it is essential to additionally incorporate dislocation structures in active learning. This requires automated generation of these structures along with computation of their DFT energies to achieve the active learning process. Consequently, it remains a significant question whether an alternative training dataset, one that eliminates the need to construct dislocation structures and is straightforward to generate automatically, can be effectively utilized to construct NNPs for dislocation plasticity in ceramics.

In this work, we propose a training dataset easy to compute via high-throughput calculation for the construction of NNPs for dislocation plasticity in ceramics, using three typical functional ceramics ZnO, GaN, and $SrTiO_3$ as prototypes. Wurtzite ZnO and GaN are direct wide bandgap semiconductors[38] with significant potential for various applications, while cubic $SrTiO_3$, a typical perovskite oxide, has high dielectric constants, making it attractive for capacitors, varistors, and more[39]. The mechanical and functional tailoring of dislocations in these three ceramics has been widely studied experimentally[10,40–44]; however, the atomic-scale mechanism remains largely unexplored. The NNPs developed in this study provide powerful tools for detailed atomistic modeling and simulation of dislocation plasticity in these three ceramics. They also suggest an effective framework to construct NNPs, opening new avenues for exploring the plastic behavior of ceramics. The dataset, easy to compute via high-throughput calculation could also be used in the on-the-fly active learning of NNP for dislocation plasticity in ceramics. For instance, the structures within this dataset can serve as candidate pools, automatically selected for inclusion in the training dataset during the active learning process.

Results

A general recipe of easy-to-compute training datasets

To address the challenge of constructing accurate dislocation core configurations and calculating their DFT energies for a training dataset, this study shifts focus from complex dislocation core structures, which necessitate large models and substantial computational resources, to simpler dislocation-related structures, that enable high-throughput DFT calculation (see Fig. 1). Ultimately, we aim to demonstrate that such simplified model datasets, excluding any dislocation core structures, can effectively describe dislocation properties and prove to be a powerful tool for developing NNPs for dislocation plasticity in ceramics.

The dislocation-related structures include uniformly deformed structures, cleavage structures, and stacking fault structures. The training dataset involving the dislocation-related structures not only eliminates the need to construct complex dislocation configurations but is also readily computable

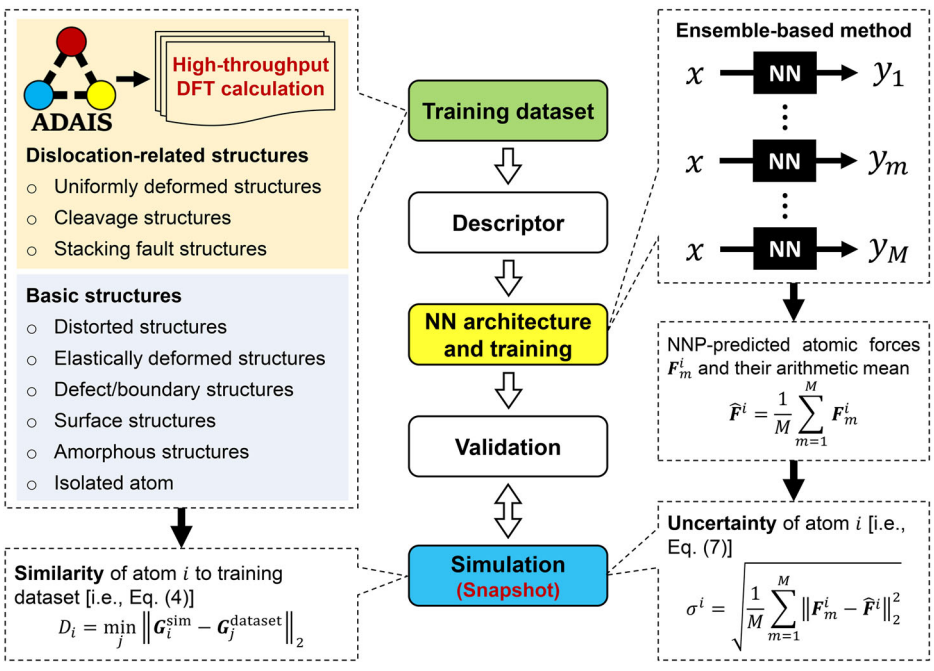

Fig. 1 | Strategy and workflow of the construction of NNP for dislocation plasticity in ceramics in this work. The dislocation-related structures were generated using our open-source ADAIS code[45] together with the VASP code[46], enabling high-throughput DFT calculations. The basic structures provide a description of the essential properties of materials, which serve as the foundation of an NNP. For more details on the implementations, workflows, and execution examples of the ADAIS code, one may refer to our previous publication[45]. In addition to the broad validation across various properties, the effectiveness of the training dataset and NNPs was further confirmed by assessing the similarity to the training dataset and evaluating the uncertainty through the ensemble-based method, using snapshots derived from large-scale simulations.

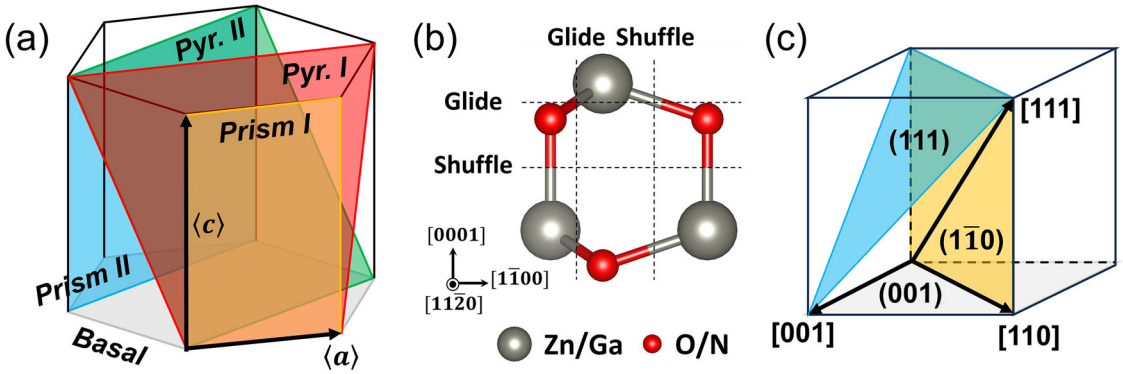

Fig. 2 | Typical slips systems in ZnO, GaN, and $SrTiO_3$. **a** Typical slip systems on the basal {0001}, prismatic I {10$\bar{1}$0}, prismatic II {11$\bar{2}$0}, pyramidal I {10$\bar{1}$1}, and pyramidal II {11$\bar{2}$2} planes in the hexagonal close packing (HCP) structure. **b** Basal and prismatic I planes of shuffle-set and glide-set in the wurtzite structure. **c** Typical slip systems on the {001}, {011}, and {111} planes in the cubic structure.

through high-throughput calculation. It is made possible by our open-source ADAIS code[45], along with the Vienna ab initio simulation package (VASP) code[46]. The ADAIS code has been designed specifically to automatically ascertain anisotropic ideal strength utilizing high-throughput DFT calculations.

Aside from the unit cell's structure files and a series of deformation directions, no additional parameters or files were required to yield the ultimate training dataset of dislocation-related structures. It is suitable for target ceramics with any crystal structure or symmetry. For more details on the implementations, workflows, and execution examples of the open-source ADAIS code, one may refer to our previous publication[45]. In comparison, models that include complex dislocation cores need to be manually constructed, as their core structures and boundary conditions must be thoroughly checked before calculating their DFT energy to serve as training datasets. Furthermore, dislocation-related structures are typically composed of only tens of atoms. These structures are considerably smaller compared to models that incorporate dislocation cores, which are typically composed of hundreds of atoms. As a result, the generation of the training dataset becomes more efficient and less computationally demanding.

These dislocation-related structures represent various modes of deformation along specific deformation directions corresponding to the slip systems of the target ceramics, thereby closely aligning with their dislocation properties. In uniformly deformed structures, all crystal cell layers are displaced uniformly along designated directions[47,48]. This study employed uniform deformations of uniaxial tension, uniaxial compression, and pure shear. In contrast, cleavage and stacking fault structures involve localized deformations in the given directions, affecting only two neighboring atomic planes while other layers maintain their original positions[47,48]. The energetics of these highly deformed structures are fundamental in describing not only the crystal instability, which leads to dislocation nucleation and cracking, but also the notably distorted atomic structure near the dislocation core.

The deformation directions were chosen based on the crystal's symmetry, usually covering all inequivalent low-index crystallographic orientations and planes, along with previously reported slip systems for the target ceramics. In this work, for wurtzite ZnO and GaN, typical deformation directions on the basal {0001}, prismatic I {10$\bar{1}$0}, prismatic II {11$\bar{2}$0}, pyramidal I {10$\bar{1}$1}, and pyramidal II {11$\bar{2}$2} planes in the hexagonal close packing (HCP) structure are considered, as shown in Fig. 2a. In the wurtzite structure, there are two different slip planes, i.e., glide-set and shuffle-set, on basal (0001) and prismatic I (10$\bar{1}$0) planes (see Fig. 2b). Several of these deformation directions have been reported in wurtzite ZnO and GaN. For instance, the {10$\bar{1}\bar{1}$}⟨$\bar{1}$2$\bar{1}$0⟩ and {0001}⟨$\bar{1}$2$\bar{1}$0⟩ slip systems were observed for {2$\bar{1}\bar{1}$0} indentation, and that for {10$\bar{1}$0} indentation was {10$\bar{1}$0}⟨$\bar{1}$2$\bar{1}$0⟩[49]. The {0001} basal and {101$\bar{1}$} pyramidal dislocations were found under {0001} indentation[50,51]. For the cubic $SrTiO_3$, the typical deformation directions on the {001}, {011}, and {111} planes were considered, as shown in Fig. 2c, several of which have been observed in cubic $SrTiO_3$. For instance, under uniaxial compression, the {110}⟨1$\bar{1}$0⟩ and {100}⟨010⟩ slip systems are activated at low and high temperatures, respectively[41]. The straight and highly ⟨111⟩-orientated ⟨110⟩-type 35.26° dislocations were found in the polished $SrTiO_3$ single crystals[52].

In addition to dislocation-related structures, the training dataset includes distorted structures, elastically deformed structures, defect/boundary structures, surface structures, amorphous structures, and isolated atoms, akin to those used in conventional NNPs. These basic structures provide a description of the essential properties of materials, such as lattice constants and elastic constants, which serve as the foundation of an NNP. The distorted structures were generated through ab initio MD simulations at finite temperatures or by applying random distortions to atoms within the structures. Unlike uniformly deformed structures, which mainly concentrate on configurations that are nearing instability, elastically deformed structures are focused on maintaining within the elastic limit. The unrelaxed surface structures are identical to the cleavage structures with a significant separation distance between the deformed neighboring planes. For further details about the training dataset, please refer to Tables S2, S6, S10 in the Supplementary Materials.

Training NNPs with small atomic structures raises concerns about their accuracy when applied to large-scale simulations. The complexity and diversity inherent in larger systems may not be adequately represented by small-scale training datasets, potentially leading to biases and inaccuracies in the simulations. As a result, the reliability of the training dataset in large-scale simulations requires further verification. In this work, beyond a broad validation across various properties, the effectiveness of our training dataset was further confirmed by measuring the similarity to the training dataset and assessing the uncertainty through an ensemble-based method[53–56], using snapshots derived from large-scale simulations (see Fig. 1).

The general recipe proposed in this work for generating easy-to-compute training datasets via high-throughput DFT calculations eliminates the need to create complex dislocation configurations, and is suitable regardless of the crystal structure and symmetry of the target ceramics. Consequently, it can be readily applied to other important ceramics, such as wurtzite AlN, InN, and SiC; cubic MgO; and cubic and tetragonal perovskite oxides like $BaTiO_3$, $KNbO_3$, $DyScO_3$, $BiFeO_3$, $MgSiO_3$, and $PbTiO_3$. Additionally, it is applicable to complex crystal structures, including ZrO_2, CeO_2, and UO_2.

Accuracy and performance of neural network potential

The accuracy and performance of the NNP were first validated across various properties, including lattice constants, elastic constants, elastic moduli, phonon dispersion, surface energy, energy under volumetric strain, cleavage energy, formation energy of planar defects, SFE, dislocation core structure, and dislocation slip barrier. The NNP's performance concerning

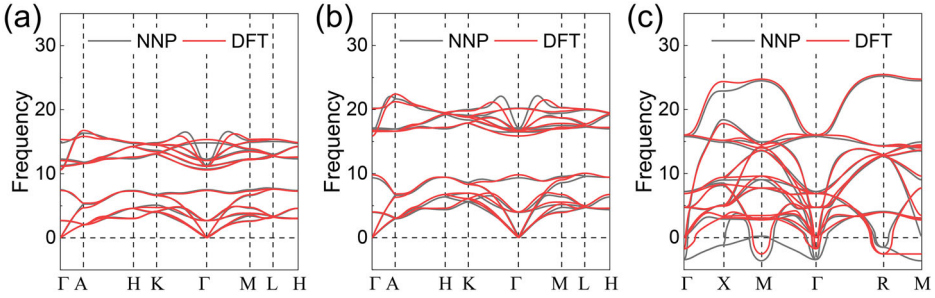

Fig. 3 | NNP performance for the phonon dispersion compared with the DFT results. a wurtzite ZnO, **b** wurtzite GaN, and **c** cubic $SrTiO_3$.

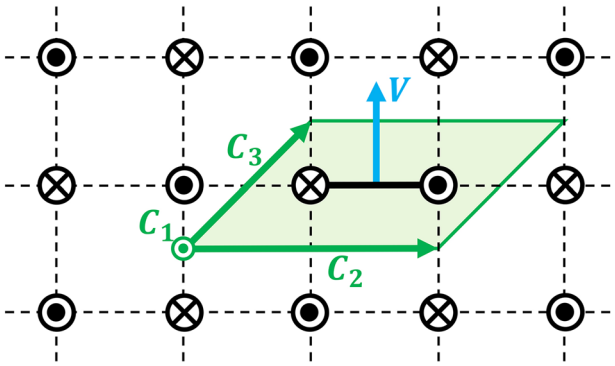

Fig. 4 | Dislocation dipole model with periodic quadrupolar arrangements used for MD simulation of dislocation. The periodic cell of the arrangement is shown by the green-shaded area, with $\boldsymbol{C}_i$ representing its periodicity vectors. The cut vector of the dislocation dipole is denoted by $\boldsymbol{V}$.

the phonon dispersion is particularly noteworthy, as depicted in Fig. 3. The phonon dispersion curves predicted by the NNP exhibit a reasonable agreement with the DFT results. In the following section, we will illustrate and discuss the performance of the NNP on dislocation-related properties. In this work, the dislocation dipole model with periodic quadrupolar arrangements[57–60] was used to determine the dislocation core structure and slip barrier (see Fig. 4). Please refer to Table 1 and the Supplementary Materials for detailed information on other validation results.

Stacking fault energy. Figure 5 illustrates the performance of the NNP in predicting the SFEs of pyramidal planes in wurtzite ZnO and GaN, compared with the results from DFT and empirical potential. Additional NNP-determined SFEs are presented in Figs. S13 and S25 in the Supplementary Materials. The NNP-predicted SFEs are in good agreement with the DFT results, providing a robust foundation for atomistic simulations of dislocation plasticity in wurtzite ZnO and GaN using these NNPs, given that the SFE is a fundamental property for dislocation nucleation and slip[61,62]. The empirical potentials considerably overestimate the SFE (see Figs. 5c, d). For instance, the predicted unstable SFE of ZnO $(10\bar{1}1)[1\bar{2}10]$ via the analytic bond-order[63] and Buckingham-type[64] empirical potentials are 2.68 and 1.68 J/m^2, respectively, significantly larger than those of DFT and NNP, which are 1.30 and 1.28 J/m^2, respectively.

Figure 6a, b illustrate the performance of the $SrTiO_3$ NNP in predicting the $(110)[1\bar{1}0]$ SFE, compared with the results from DFT and the pair empirical potential[65]. The NNP results align well with the DFT results, whereas the pair empirical potential[65] overestimates the SFE. The formation of a nonstoichiometric stacking fault in cubic $SrTiO_3$ through the dissociation of a [012] dislocation, where two (001) Ti-O layers end up neighboring across the stacking fault plane due to the absence of a (001) Sr-O layer, has been reported[66], as depicted in Fig. 6c. Figure 6d presents the relative energies of the stacking faults with respect to the most stable configuration that features a 1/2[010] displacement component (see Fig. 6c). The NNP results agree well with the DFT results, even though these results were not included in the training dataset. The pair empirical potential[65] fails to predict this nonstoichiometric model. Other SFE results predicted by the NNP are presented in Fig. S34 in the Supplementary Materials, demonstrating good agreement with the DFT results.

Dislocation in wurtzite ZnO and GaN. Figure 7a, b depict the atomic structure of a basal glide-set 60° partial dislocation dipole in wurtzite ZnO, with a stacking fault situated between two partials. Each partial has an extra Zn or O atom at the dislocation core, referred to as the Zn core and O core, respectively. These nonstoichiometric dislocation cores are charged. To demonstrate the performance of the NNP for the charged dislocation cores and the long-range electrostatic interaction between them, one partial dislocation in the dipole model was displaced by a distance d (see Fig. 7c). The resulting energy change, ΔE^{total}, originates from three sources: (1) the elastic interaction between dislocations, $\Delta E^{\text{elastic}}$; (2) the SFE due to the change in the area of the stacking fault, ΔE^{SFE}; and (3) the long-range electrostatic interaction between the charged dislocations, $\Delta E^{\text{electro}}$.

In this study, we determined the extra charge at the dislocation core through Bader charge analysis[67] after DFT static calculation, yielding values of $+0.88e$ and $-0.88e$ for the Zn and O cores, respectively. We then calculated $\Delta E^{\text{electro}}$ using the Ewald summation[68] with setting two virtual charged atoms ($\pm 0.88e$) at the positions of the dislocation core. Figure 7d presents the energy change ΔE^{total} calculated by the NNP and DFT using a dipole model of $(n, m) = (12,4)$. The NNP results align well with the DFT results. It is important to note that the training dataset did not include these dislocation structures. The discrepancy between the NNP and DFT results is significantly smaller than $\Delta E^{\text{electro}}$ (see Fig. 7d), suggesting that the NNP can accurately account for the long-range electrostatic interaction, which is not truncated at the cutoff radius, even though the charge information is not included in the NNP. It's worth noting that the minimum distance between two charged partial dislocations is ~12 Å at $d = \pm 4(a/2)$, which is significantly larger than the cutoff radius of NNP (i.e., 7.0 Å).

The accuracy of the NNP has recently been further enhanced by employing additional neural networks to construct environment-dependent atomic charges, thereby explicitly accounting for long-range electrostatic interactions[23,69]. As demonstrated in this work, even for systems with substantial charge transfer between atoms, such as nonstoichiometric dislocation core structures, long-range electrostatic interactions can be captured with high accuracy in an effectively screened manner by short-ranged NNPs. Moreover, explicitly including electrostatic interactions using the atomic charges increases the computational costs of NNP because a second set of neural networks is introduced[23,69], and an Ewald summation[68] or PPPM solver[70] has to be used to calculate the electrostatic energies and forces. Therefore, in this study, we employed short-ranged NNPs and achieved excellent accuracy compared to DFT results, even for nonstoichiometric and charged dislocation core structures.

The Peierls potential of the basal glide-set 60° partial dislocation in ZnO, as calculated through NNP and DFT, is illustrated in Fig. 8a. The results presented herein are the average values for the dislocations with O core and Zn core. The Peierls barrier, as determined through ZnO NNP, is

Table 1 | NNP and DFT predicted lattice constants (*a* and *c* in Å), elastic constants (c_{ij} in GPa), polycrystalline shear (μ) and bulk (κ) moduli (in GPa) of wurtzite ZnO, wurtzite GaN and cubic $SrTiO_3$

	a	*c*	c_{11}	c_{12}	c_{13}	c_{33}	c_{44}	c_{66}	μ	κ	Note
wurtzite ZnO	3.287	5.305	201	120	101	213	38	41	43.42	129.17	This work, NNP
	3.287	5.306	188	107	94	201	37	40	41.22	129.59	This work, GGA-PBE
	3.278	5.291									GGA-PBE[23]
			191.5	108.7	95	206.7	41.4	38			PBE[110]
			221.1	105.9	87.4	234.3	57.6	53.4			PBE+U[110]
	3.195	5.160									LDA[111]
	3.148	5.074									LDA+U[111]
	3.25	5.21									Exp.[112]
			190	110	90	196	39	40			Exp.[112]
			206	117	118	211	44.3	44.6			Exp.[113]
			209.7	121.1	105.1	210.9	42.47	44.29			Exp.[114]
wurtzite GaN	3.224	5.290	335	143	123	392	79	92	93.38	204.25	This work, NNP
	3.248	5.282	329	128	96	355	86	100	99.42	183.44	This work, GGA-PBE
			356	146	115	382	91	105		205	LDA[115]
	3.190	5.189									Exp.[116]
	3.189	5.178									Exp.[117]
			390	145	106	398	105	123			Exp.[118]
cubic $SrTiO_3$	3.901		331	106			98		109.20	189.00	This work, NNP
	3.895		351	103			114		118.03	186.04	This work, GGA-PBEsol
			319.3	97.5			113				GGA-PBE[119]
			290.7	93.9			110.9				BLYP[119]
	3.895		352	105			116				GGA-PBEsol[28]
			317.2	102.5			122.35				Exp.[120]

The theoretical values and experimental data previously published in the literature are also shown for comparison.

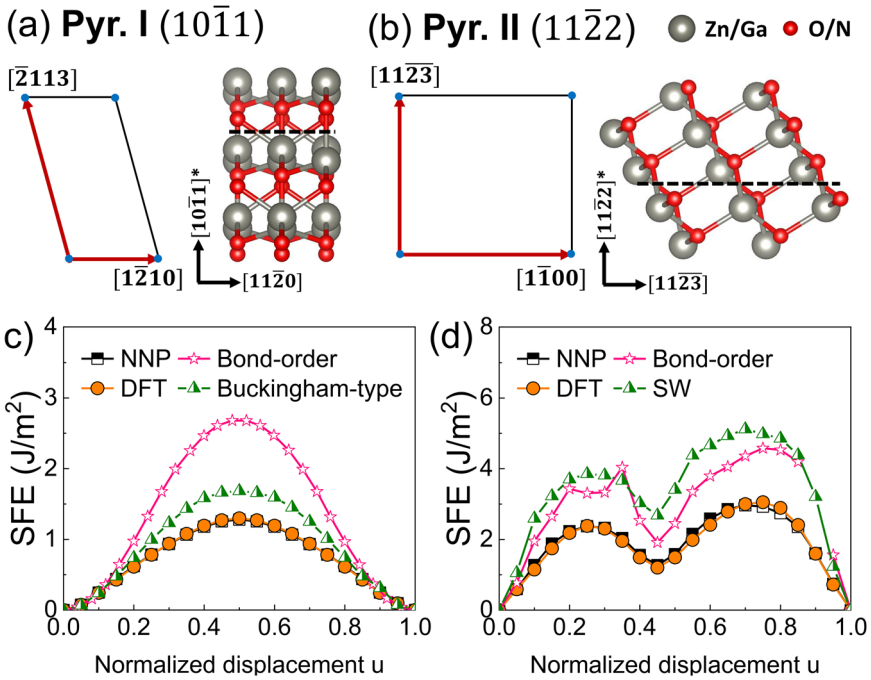

Fig. 5 | Accuracy and performance of NNP on the SFEs of ZnO and GaN. a, **b** Diagrams depicting **a** pyramidal I and **b** pyramidal II planes in the wurtzite structure. The in-plane lattices are accentuated by red lines, and the slip planes are underscored by black dashed lines. **c**, **d** The calculated SFEs of the pyramidal planes using NNP, DFT, and empirical potentials for **c** ZnO (10$\bar{1}$1)[1$\bar{2}$10], and **d** GaN (11$\bar{2}$2)[11$\bar{2}$3]. The analytic bond-order[63] and Buckingham-type[64] empirical potentials of ZnO, as well as the analytic bond-order[121] and SW[122] empirical potentials of GaN, were employed for comparison.

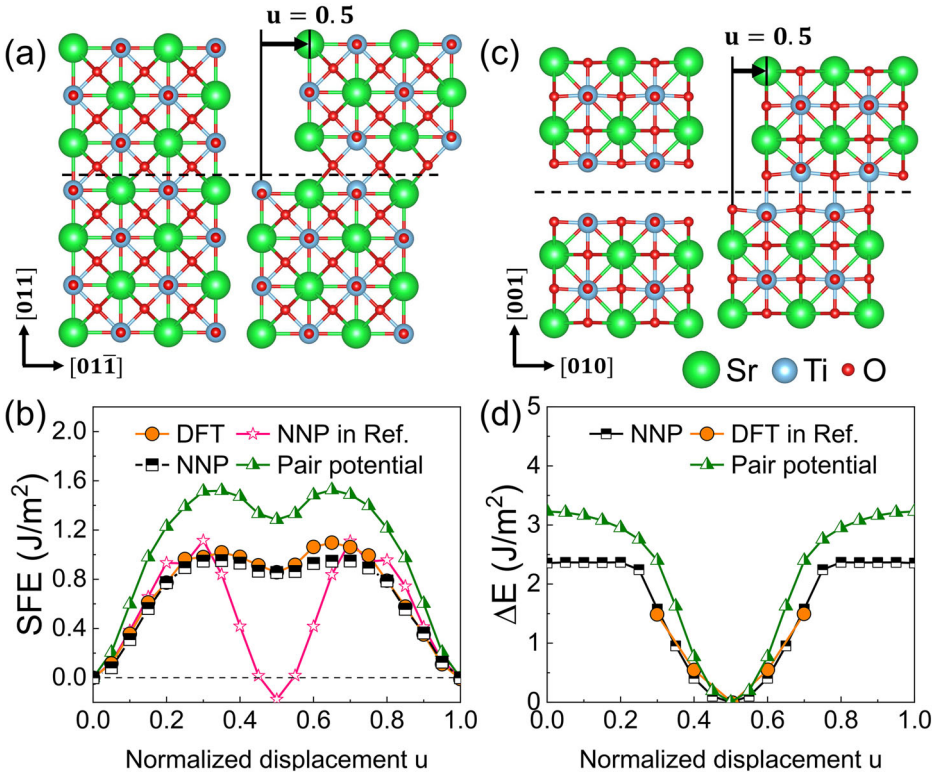

Fig. 6 | Accuracy and performance of NNP on the SFEs of $SrTiO_3$. **a** Structures and **b** energy profile of the (110)[1$\bar{1}$0] stacking fault in cubic $SrTiO_3$, as calculated by NNP, DFT, and pair empirical potential. **c** Nonstoichiometric stacking fault formed with the dissociation of [012] dislocation in cubic $SrTiO_3$[66], where two (001) Ti-O layers are positioned as neighbors across the stacking fault plane due to the absence of a (001) Sr-O layer. **d** Relative energies of the stacking faults compared to the most stable configuration, which includes a 1/2[010] displacement component (i.e., $u = 0.5$). The results of the pair empirical potential[65], NNP in ref. 28, and DFT in ref. 66 are shown for comparison. Black dashed lines in (**a**, **c**) highlight the slip planes.

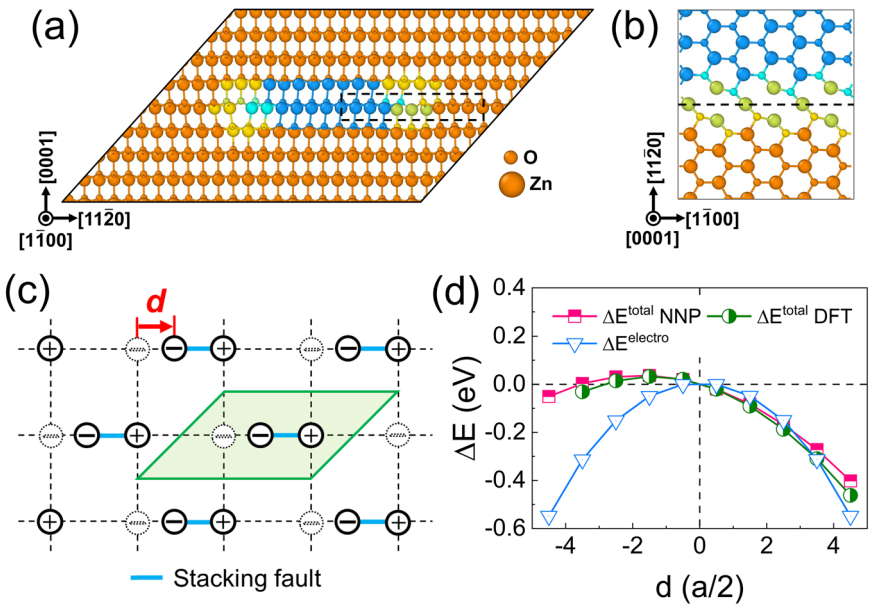

Fig. 7 | Accuracy and performance of NNP on the dislocation in ZnO. **a**, **b** Atomic structure of the basal glide-set 60° partial dislocation dipole with Zn core and O core: **a** viewed along the dislocation line, and **b** viewed perpendicular to the (0001) plane of the region outlined by the black dashed rectangle in (**a**). The black broken line in (**b**) represents dislocation lines along the cores. **c** Dislocation dipole model with periodic quadrupolar arrangements composed of positively charged (Zn core) and negatively charged (O core) basal glide-set 60° partial dislocations, where one dislocation is displaced by a distance d from its initial position. The periodic cell of the arrangement is shown by the green-shaded area. **d** Energy change ΔE of the dislocation dipole model as a function of the displacement d, with a model size of $(n, m) = (12,4)$.

0.018 eV/Å, a value that closely aligns with the DFT result of 0.017 eV/Å via a simulation cell of $(n, m) = (12,4)$. Figure 8c shows the average value of the Peierls potential for the basal glide-set 60° partial dislocations with N core and Ga core in GaN. The Peierls barrier of GaN, at 0.054 eV/Å (NNP) and 0.062 eV/Å (DFT) with a model size of $(n, m) = (12,4)$, significantly exceeds that of ZnO.

The Peierls potential of the dislocation with either an O core, Zn core, N core, or Ga core was also calculated within a large dipole model of $(n, m) = (48,16)$, where only one dislocation was moved. In a model of this size, the variations in elastic and electrostatic interactions, as the distance between two partial dislocations shifts, are negligible. Along the directions of stacking fault growth and decline, there is a difference in the Peierls barrier and Peierls stress of the partial dislocation. Owing to the positive SFE, the Peierls barrier and Peierls stress are more pronounced along the stacking fault growth directions. As shown in Fig. 8b, d, the basal glide-set 60° partial dislocation with O core or N core, i.e., 0.011 eV/Å for O core and 0.044 eV/Å for N core, has a smaller Peierls barrier compared to the dislocation with Zn core or Ga core (0.029 eV/Å for Zn core and 0.061 eV/Å for Ga core) along the stacking fault growth direction. Utilizing Eq. (2), the Peierls stresses along the direction of stacking fault growth are determined to be 1.2 and 3.8 GPa for O core and Zn core in ZnO, and 6.4 and 9.4 GPa for N core and Ga core in GaN, respectively.

Dislocation in cubic $SrTiO_3$. The ⟨001⟩ edge dislocation with a ⟨001⟩ Burgers vector, {110} glide plane, and ⟨1$\bar{1}$0⟩ line vector has been investigated in experiment[71]. Upon inserting the ⟨001⟩ edge dislocation dipole, as shown in Fig. 9a–c, the dislocation cores are found to be polar. They consist of alternating $(SrTiO_2)^{2+}$ layers (see Fig. 9a) and $(SrTiO_4)^{2-}$ layers (see Fig. 9b). A charge balance was achieved by moving one of the two extra oxygen atoms along the [1$\bar{1}$0] column from the negatively charged core to the positively charged core, resulting in two reconstructed and nonpolar dislocations.

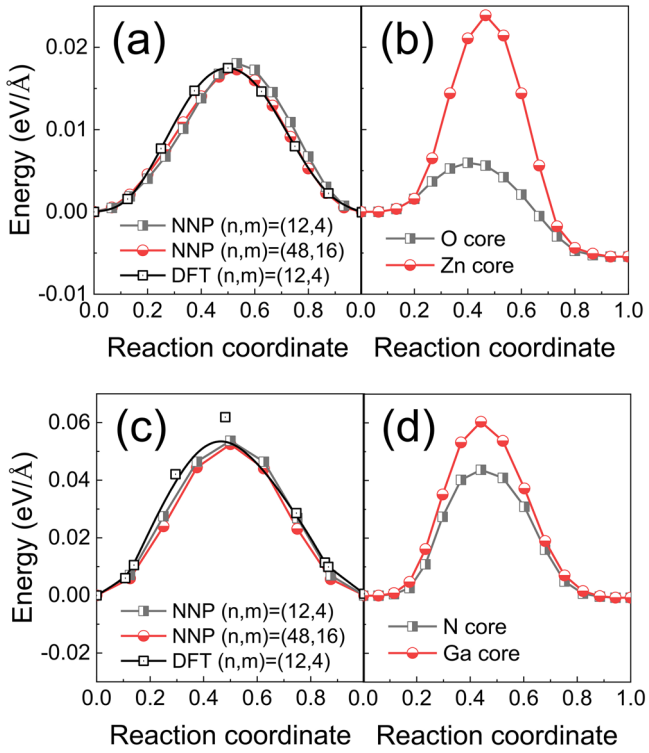

Fig. 8 | Accuracy and performance of NNP on the dislocation in ZnO and GaN. Peierl potential of the basal glide-set 60° partial dislocation for **a**, **b** ZnO and **c**, **d** GaN, calculated using the dislocation dipole models and the NEB method. **a**, **c** Average values of the Peierls potential for the dislocations with O core and Zn core in ZnO (**a**), as well as those with N core and Ga core in GaN (**c**). **b**, **d** The Peierls potential of the dislocation with either an O core, Zn core, N core, or Ga core, which was calculated by moving only one dislocation within a large dipole model of (*n*, *m*) = (48,16). The DFT results are provided for comparison.

The energy difference between the dislocation dipole models before and after charge balance originates from two factors: (1) the core energy, resulting from the reconstruction of the dislocation core structure after charge balance (ΔE^{core}), which is model-size independent; and (2) the long-range electrostatic interaction between charged dislocations ($\Delta E^{electro}$). Upon achieving charge balance, the long-range electrostatic interaction significantly diminishes. As the model size increases, $\Delta E^{electro}$ decreases, and with an infinite model, $\Delta E^{electro} \to 0$. The elastic interaction of the dislocation dipole models before and after charge balance, which is a function of the Burgers vector and the distance between dislocations[72], is assumed to be equal (i.e., $\Delta E^{elastic} = 0$) as the Burgers vector and the distance between dislocations remain unchanged.

Figure 9e presents the results of the energy difference between the dislocation dipole models before and after charge balance as a function of the distance x defined in Fig. 9d. The energy difference ΔE, as determined by NNP, is −0.17 eV/Å at x = 29 Å. This aligns closely with the DFT result of −0.18 eV/Å and converges towards the ΔE^{core}, i.e., −0.37 eV/Å, as the model size increases. The negative value of ΔE^{core} suggests that the charge-balanced ⟨100⟩ edge dislocation is more stable compared to its counterpart without charge balance. The $\Delta E^{electro} = \Delta E^{total} - \Delta E^{core}$ decreases from 0.20 eV/Å at the distance x = 29 Å to ~0 at the distance x = 91 Å. The energy difference predicted by the pair empirical potential does not converge at a distance x greater than 400 Å (see Fig. 9e), as the $\Delta E^{electro}$ encompasses not only the electrostatic interaction between the charged dislocation cores, but also the electrostatic interaction between the charged dislocation core and each atom with a fixed charge.

The dislocation with a ⟨110⟩ Burgers vector, {1$\bar{1}$0} glide plane and ⟨111⟩ line vector, and thus, of mixed character, has been reported in experimental studies[52]. The Burgers vector can be decomposed into its edge (1/3⟨11$\bar{2}$⟩) and screw (2/3⟨111⟩) components. As depicted in Fig. 10a–c, the charged ⟨110⟩ mixed dislocation dipole was initially inserted, followed by a charge balance operation moving one of the extra oxygen atoms from the negatively charged core to the positively charged core.

Owing to the presence of the stable SFE (see Fig. 6b), the ⟨110⟩ mixed dislocation tends to split into two partials with a 1/2⟨110⟩ Burgers vector on a {1$\bar{1}$0} plane, thereby creating a stacking fault on this plane. Fig. 10d illustrates the optimal configuration of ⟨110⟩ mixed dislocations. The splitting distance is ~24 Å, which aligns closely with the experimental results of 25 Å[52]. The stable SFE (850 mJ/m^2) predicted by NNP and DFT is comparable to those estimated in the experiment, i.e., 606.087 ± 76.66 mJ/m^2. In comparison, due to the larger stable SFE of 1280 mJ/m^2 predicted by the pair empirical potential[65], the splitting distance is 12 Å.

Plastic deformation tests and experimental comparisons

Compression of *c*-oriented GaN nanopillar. Figure 11 illustrates the snapshots of the atomic configuration of *c*-oriented GaN nanopillar

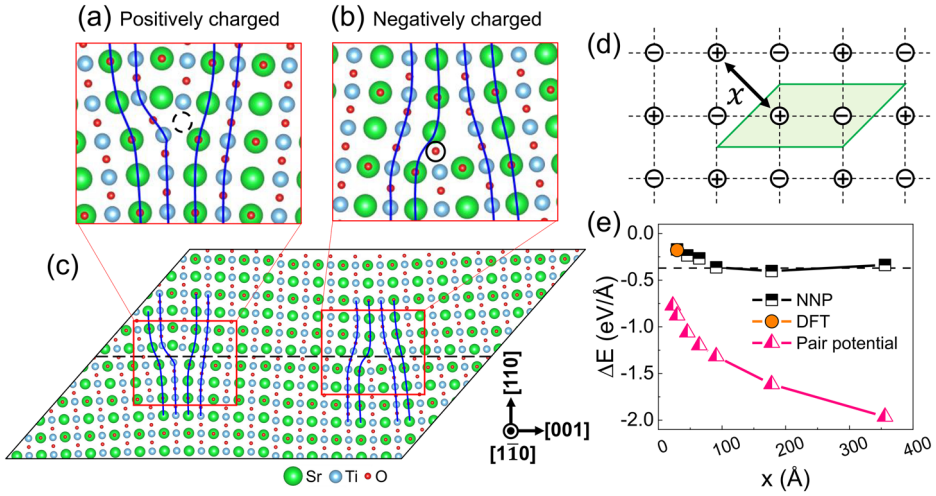

Fig. 9 | Accuracy and performance of NNP on the dislocation in $SrTiO_3$. **a** Positively and **b** negatively charged ⟨001⟩ edge dislocations in **c** the dislocation dipole model, which has a ⟨1$\bar{1}$0⟩ line vector and a {110} slip plane. For the charge-balanced dislocation core, one of the two extra oxygen atoms along the [1$\bar{1}$0] column was relocated from the position marked by the solid circle in (**b**) to the position indicated by the dashed circle in (**a**). **d** Dislocation dipole model with periodic quadrupolar arrangements, comprising positively and negatively charged dislocations, which result in long-range electrostatic interaction. The periodic cell of the arrangement is delineated by the green-shaded area. **e** Energy difference ΔE between the dislocation dipole models before and after charge balance as a function of the distance x defined in (**d**). The results of DFT and pair empirical potential[65] are also shown for comparison.

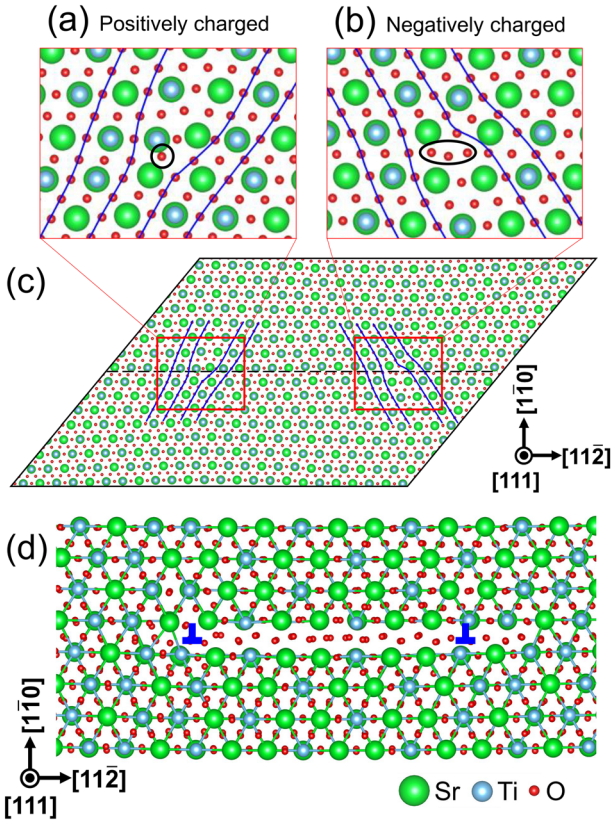

Fig. 10 | Accuracy and performance of NNP on the dislocation in $SrTiO_3$. **a** Positively and **b** negatively charged ⟨110⟩ mixed full dislocations in **c** the dislocation dipole model, which has a ⟨111⟩ line vector and a {1$\bar{1}$0} slip plane. Black circles highlight the oxygen atoms at the dislocation core. For the charge-balanced dislocation core, one of the extra oxygen atoms at the dislocation core was moved from (**b**) to (**a**). **d** Charge-balanced ⟨110⟩ mixed dislocation in its glide dissociated form, cut from a larger dislocation dipole model. The locations of partial dislocations, determined based on the Sr-O FCC sublattice via the dislocation extraction algorithm (DXA)[95], are highlighted by blue ⊥ symbols.

under a compressive engineering strain $\varepsilon = -0.1164$, projected along [1$\bar{1}$00] and [0$\bar{1}$10]. The 1/3⟨1$\bar{2}$13⟩ dislocations are activated, and their slip planes have an angle of ~58° with respect to the basal plane (highlighted by black dashed lines in Fig. 11c, e). It is indicated that the primary slip system is on the pyramidal II plane. This is in good agreement with experimental results[73], which found that the first formed dislocations in microcompressed *c*-oriented GaN micropillars are 1/3⟨11$\bar{2}\bar{3}$⟩{11$\bar{2}$2} dislocations. A secondary slip band oriented at an angle of ~72° relative to the basal plane was also observed experimentally, with a Burgers vector of 1/3⟨1$\bar{2}$13⟩[73]. It doesn't match any major slip system in GaN. As shown in Fig. 11e, f, similar secondary slip planes were also observed, highlighted by the red dashed lines. It is found the secondary slip planes are also the pyramidal II planes but not parallel with the view direction [0$\bar{1}$10], showing an angle of ~70° from the basal plane. Our simulation results suggest a plausible interpretation for the experimentally observed secondary slip band[73]. The compression simulation of the *c*-oriented GaN nanopillar with the same parameters was also performed using the SW empirical potential for comparison. The results are shown in Fig. S1 in the Supplementary Materials. No obvious pyramidal dislocation is observed due to the overestimated SFE by this empirical potential, as shown in Fig. 5d.

Nanoindentation of (0001)-oriented ZnO. Figure 12 displays snapshots of dislocation structures of wurtzite ZnO under (0001) nanoindentation, indicating that basal and pyramidal dislocations nucleate and slip. It is in good agreement with experimental results[50,74–76]. In detail, the basal dislocation includes both the basal shuffle-set 1/3⟨11$\bar{2}$0⟩ full dislocation and the basal glide-set 1/3⟨1$\bar{1}$00⟩ partial dislocation. The primary pyramidal dislocation is the 1/3⟨1$\bar{2}$13⟩ dislocation on the pyramidal I plane, and it aligns ~60° to the (0001) surface. A few dislocations on the pyramidal II plane are also observed, as shown in Fig. 12d. The nanoindentation simulation with the same parameters was also performed using the Buckingham-type empirical potential for comparison. The results are shown in Fig. S2 in the Supplementary Materials. There is little pyramidal dislocation observed due to the overestimated SFE by this empirical potential (see Fig. 5c).

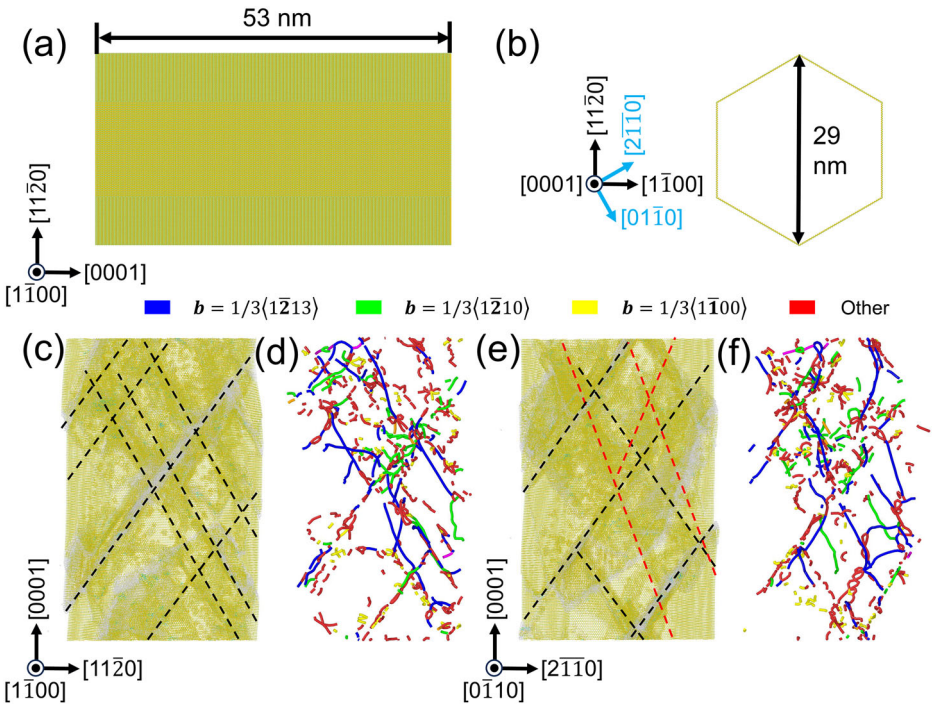

Fig. 11 | Compression of *c*-oriented GaN nanopillar. **a**, **b** Model of a *c*-oriented GaN nanopillar. **c**–**f** Snapshots of atomic configurations under a compressive engineering strain of $\varepsilon = -0.1164$, projected along **c**, **d** [1$\bar{1}$00] and **e**, **f** [0$\bar{1}$10]. They were analyzed via (**c**, **e**) the identify diamond structure (IDS) method[94], and (**d**, **f**) the dislocation extraction algorithm (DXA)[95] based on the Ga HCP sublattice. The slip planes are highlighted by black and red dashed lines, with angles of approximately 58° and 70° from the basal plane, respectively. Atoms within perfect wurtzite structures are not shown in (**a**–**c**, **e**).

Atomic environment similarity and atomic force uncertainty

As discussed in section "A general recipe of easy-to-compute training datasets", training NNPs with small atomic structures often prompts questions about their accuracy in large-scale simulations. Therefore, in this work, we further validated the effectiveness of the training dataset and NNPs through similarity measurement and uncertainty quantification. The similarity measures the minimum distance D^i of the local atomic environment between the atom i in the lager-scale simulation and any atoms in the training dataset (i.e., Eq. (4)). NNPs usually provide more reliable predictions for structures that exhibit higher similarity to the training dataset.

Figure 13a shows the maximum value of D^i, denoted as $\max\{D^i\}$, in the dipole model of basal shuffle-set $1/3\langle 11\bar{2}0\rangle$ edge dislocation with reference to different sets of structures within the training dataset. The dipole models were relaxed by DFT at initial and saddle configurations as the dislocation slipped along the $[11\bar{2}0]$ directions. The inclusion of stacking fault structures significantly increases the similarity between the training dataset and the dislocation core structures, compared to using only basic structures. It is evident as the value of $\max\{D^i\}$ decreases from 1.67 to 1.04 for the initial configuration. Furthermore, the similarity quantified by D^i for atoms in the snapshot of the ZnO (0001) nanoindentation simulation is displayed in Fig. 13c, d. Corresponding results for GaN NNP and $SrTiO_3$ NNP can be found in Figs. S3 and S4 in the Supplementary Materials. The inclusion of dislocation-related structures, particularly the uniformly deformed structures, effectively enhances the similarity, indicated by a decrease in the value of D^i, between the training dataset and the defected structures where dislocations nucleate and slip. The inclusion of cleavage structures in the training dataset has little effect on the similarity of the dislocation core structures and nanoindentation snapshots shown in Fig. 13. Nonetheless, it could be beneficial for other forms of ceramic dislocation plasticity simulations, e.g., dislocation emission from a notch or crack tip. Therefore, our training dataset is highly optimized and effective, maintaining a minimal yet sufficient size, to construct the NNP for dislocation plasticity in ceramics.

Given a specific training set, multiple well-trained NNPs typically provide similar predictions near existing samples. However, their predictions can diverge significantly in areas far from the existing data, serving as a basis for approximate, yet useful, uncertainty quantification of NNPs[53–56]. This uncertainty offers an estimation of the reliability of NNPs for new and unseen configurations in large-scale systems. In this work, the uncertainty σ^i of atom i was determined through the variances of the predicted atomic forces by the NNPs in an ensemble (see Eq. (7)).

As shown in Fig. 13b, the NNPs constructed using a training dataset that includes both basic and dislocation-related structures effectively describe the core structure with an uncertainty smaller than 40 meV/Å. For the atoms in the defected structures in the snapshot of ZnO (0001) nanoindentation simulation, the value of uncertainty σ^i ranging from 10^1 to 10^2 meV/Å is one to two orders of magnitude smaller than the magnitude of the atomic force $\left\|\boldsymbol{F}_*^i\right\|_2$, which ranges from 10^2 to 10^3 meV/Å (see Fig. 13e). Here, $\boldsymbol{F}_*^i$ represents the atomic force vector predicted by the NNP used to perform the nanoindentation simulation. All of these results reveal that the developed NNPs show reliable prediction (i.e., less uncertainty) for new and unseen configurations in large-scale systems.

Furthermore, the scatter plot of σ^i and D^i is shown in Fig. 13f for ZnO NNP and in Fig. S3d in the Supplementary Materials for GaN NNP, suggesting that there is not a strong correlation between similarity and uncertainty, with considerable deviation observed. While NNPs typically provide more reliable predictions (i.e., lower uncertainty) for structures with higher similarity to the training dataset, as indicated by a lower D^i value, both similarity and uncertainty metrics are necessary to validate the reliability of NNPs in large-scale simulations.

Discussion

In this work, we demonstrated the construction of NNP for dislocation plasticity in ceramics, using the dislocation-related structures as a training dataset, which eliminates the need to construct complex dislocation core structures and are readily computable through high-throughput calculation. The complex nature of dislocation cores in ceramics, along with the need for expansive models often composed of hundreds of atoms for dislocation modeling, make the creation of dislocation structures and the computation of DFT energy for training datasets a demanding task. Our proposed dataset effectively addresses these challenges.

The effectiveness of our dataset was validated by the accuracy and performance of the developed NNPs across various properties, especially those not included in the training dataset. Examples include the SFE of pyramidal I and II planes, and the charged core structures and slip barriers of dislocations in wurtzite ZnO and GaN. Furthermore, Fig. 6b shows the SFE results calculated using the NNP from ref. 28, developed without dislocation-related structures in the training dataset. While this NNP accurately describes the structural phase transitions in $SrTiO_3$, its failure to predict SFE highlights the importance of including dislocation-related structures in the training dataset, as proposed in this study. By initializing with this NNP and adding dislocation-related structures as a training dataset, a new NNP was constructed, demonstrating excellent performance for the nonstoichiometric stacking fault and dislocation core structures, which were not included in the training dataset. The effectiveness of our dataset was further validated by measuring the similarity of snapshots derived from large-scale simulations to the training dataset and assessing the uncertainty of the developed NNPs for new and unseen configurations in large-scale systems. The dislocation-related structures effectively enhance the similarity between the training dataset and the defected structures where dislocations nucleate and slip. The developed NNPs show reliable prediction (i.e., less uncertainty) for new and unseen configurations in large-scale systems.

Overall, the training dataset proposed in this work accurately represents the structures under dislocation-dominated plastic deformation in ceramics, and provides an effective framework for constructing NNPs that enable the detailed atomistic modeling of ceramic plasticity, opening new avenues for exploring the plastic behavior of ceramics. This straightforward dataset can be easily created using our open-source code ADAIS, regardless of the crystal structure and symmetry of the target ceramics. The dataset easy to compute via high-throughput calculation could also be used in the on-the-fly active learning of NNP for dislocation plasticity in ceramics.

Methods

Details of NNP training

The DeepMD-kit software package[77,78] was employed to construct the NNP. 20% training dataset was randomly selected as a testing set to determine the occurrence of overfitting. The ZnO and GaN NNPs were entirely newly trained, whereas the training of $SrTiO_3$ NNP was initialized with the existing $SrTiO_3$ NNP reported in ref. 28. The training parameters are detailed in Table S1 in the Supplementary Materials. The root mean square errors (RMSEs) of energy and atomic force are 3.5 meV/atom and 57.2 meV/Å for the ZnO NNP, 5.5 meV/atom and 84.7 meV/Å for the GaN NNP, and 2.5 meV/atom and 89.6 meV/Å for the $SrTiO_3$ NNP, respectively.

Tables S2, S6, and S10 in the Supplementary Materials list the training dataset used to construct the NNPs of ZnO, GaN, and $SrTiO_3$, all of which were calculated via DFT calculations. Three typical ZnO polymorphs were considered, including cubic rocksalt (B1), cubic zinc-blende (B3), and hexagonal wurtzite (B4), as shown in Fig. S5 in the Supplementary Materials. At ambient conditions, the thermodynamically stable phase is wurtzite[79]. Zinc-blende ZnO can be stabilized only by growth on cubic substrates, and rocksalt ZnO may be obtained at relatively high pressures[79]. Two typical GaN polymorphs were considered, including cubic zinc-blende (B3) and hexagonal wurtzite (B4), as shown in Fig. S19 in the Supplementary Materials. GaN usually crystallizes in the wurtzite structure at ambient conditions, but GaN thin films grown epitaxially on various substrates have been reported to be in the zinc-blende structure[80,81]. Two typical $SrTiO_3$ polymorphs were considered, including cubic ($Pm\bar{3}m$) and tetragonal ($I4/mcm$) phases, as shown in Fig. S28 in the Supplementary Materials. At room temperature, $SrTiO_3$ has a cubic structure. Below 105 K, it undergoes an

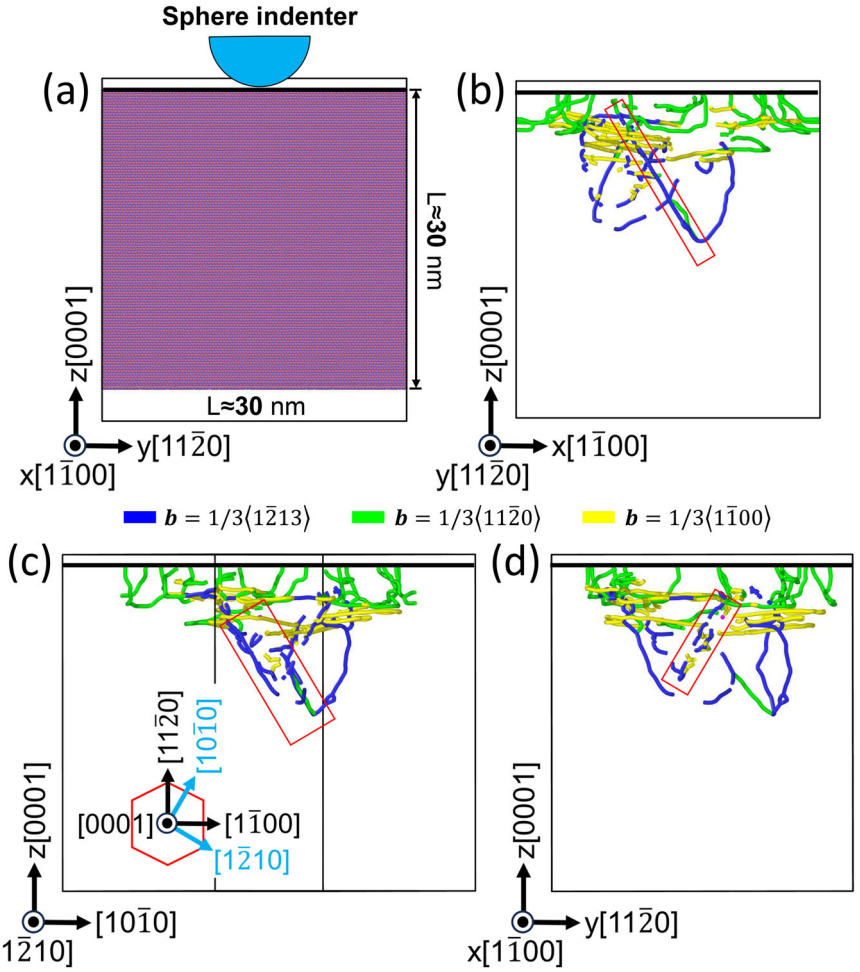

Fig. 12 | Nanoindentation of (0001)-oriented ZnO. a (0001)-oriented ZnO slab model used in the nanoindentation simulation. **b–d** Snapshot of dislocation structures at an indentation depth $h = 5.0$ nm, projected along **b** [11$\bar{2}$0], **c** [1$\bar{2}$10], and **d** [1$\bar{1}$00] directions. The slip planes that are parallel to the projection direction are emphasized with red rectangles.

antiferrodistortive structural transition, transforming to the tetragonal phase[82,83].

Density functional theory calculation

Our DFT calculations were performed using the Vienna ab initio simulation package (VASP) code[46]. We employed the projector augmented wave (PAW) method[84] with the Perdew–Burke–Ernzerhof (PBE) version[85] of the generalized gradient approximation (GGA) as the exchange-correlation functional for ZnO and GaN. In the case of $SrTiO_3$, we utilized the Perdew–Berke–Ernzerhof revised for solids (PBEsol)[86]. An energy cutoff of 520 eV (500 eV) was applied for ZnO and GaN ($SrTiO_3$). We chose an energy convergence criterion of 10^{-6} eV/cell and the Gaussian method[87] with a smearing width of 0.01 eV for the electronic self-consistency calculation. A force convergence criterion of 10^{-3} eV/Å was implemented for ionic relaxation. The Monkhorst–Pack k-mesh[88] was used with 6000 k-points per reciprocal atom (KPPRA)[89,90] for ZnO and GaN, and with KSPACING of 0.15 for $SrTiO_3$. We determined the elastic constants via the AELAS code[90], and calculated the polycrystalline bulk and shear moduli using the Voigt–Reuss–Hill approximation[91,92]. Table 1 presents the lattice constant, elastic constant, and elastic moduli, all of which align excellently with previously published theoretical values and experimental data, thereby validating the DFT parameters used in this work.

Molecular dynamics simulation

All MD simulations were performed using the large-scale atomic/molecular massively parallel simulator (LAMMPS) code[93]. We analyzed and visualized atomic configurations of dislocation with the identify diamond structure (IDS)[94] and dislocation extraction algorithm (DXA)[95] tools of the OVITO program[96]. The phonon dispersion curve was calculated via a combination of phonoLAMMPS[97] and PHONOPY[98].

The dislocation core structure and slip barrier were studied via the dislocation dipole model with periodic quadrupolar arrangements[57–60] as shown in Fig. 4. The periodicity vectors $\boldsymbol{C}_1$, $\boldsymbol{C}_2$, and $\boldsymbol{C}_3$ are defined from the unit vectors $\boldsymbol{a}_1$, $\boldsymbol{a}_2$, and $\boldsymbol{a}_3$, i.e., $\boldsymbol{C}_1 = \boldsymbol{a}_1$, $\boldsymbol{C}_2 = n\boldsymbol{a}_2$, and $\boldsymbol{C}_3 = \frac{n}{2}\boldsymbol{a}_2 + m\boldsymbol{a}_3$, where the dislocation line is parallel with $\boldsymbol{C}_1$. In addition, a homogeneous strain $\boldsymbol{\varepsilon}_{\mathrm{pl}}$ needs to be applied to the simulation cell to accommodate the plastic strain created by the dislocation dipole[99,100] as

$$\boldsymbol{\varepsilon}_{\mathrm{pl}} = \frac{1}{2\Omega}(\boldsymbol{b} \otimes \boldsymbol{V} + \boldsymbol{V} \otimes \boldsymbol{b}) \tag{1}$$

where $\otimes$ is the tensor product, $\Omega = (\boldsymbol{C}_1 \times \boldsymbol{C}_2) \cdot \boldsymbol{C}_3$ is the supercell volume, $\boldsymbol{b}$ is the Burgers vector, and $\boldsymbol{V}$ is the cut vector of the dislocation dipole (see Fig. 4), whose magnitude is the area of the cut and whose direction is normal to the cut plane.

We constructed the initial atomic structure of the dislocation using the elastic displacements of the Volterra dislocation, which are exact at large distances from the dislocation core but are only approximate near the core. The structures of the dislocation dipole are then relaxed within a fixed cell.

By applying the nudged elastic band (NEB) method[101–103], we can derive the Peierls potential, which is the dislocation energy $E_{\mathrm{disl}}(x)$ as a function of its core center position x along the slip direction. From this Peierls potential, we can then estimate the Peierls barrier E_{P} and Peierls stress τ_{P}[104,105]

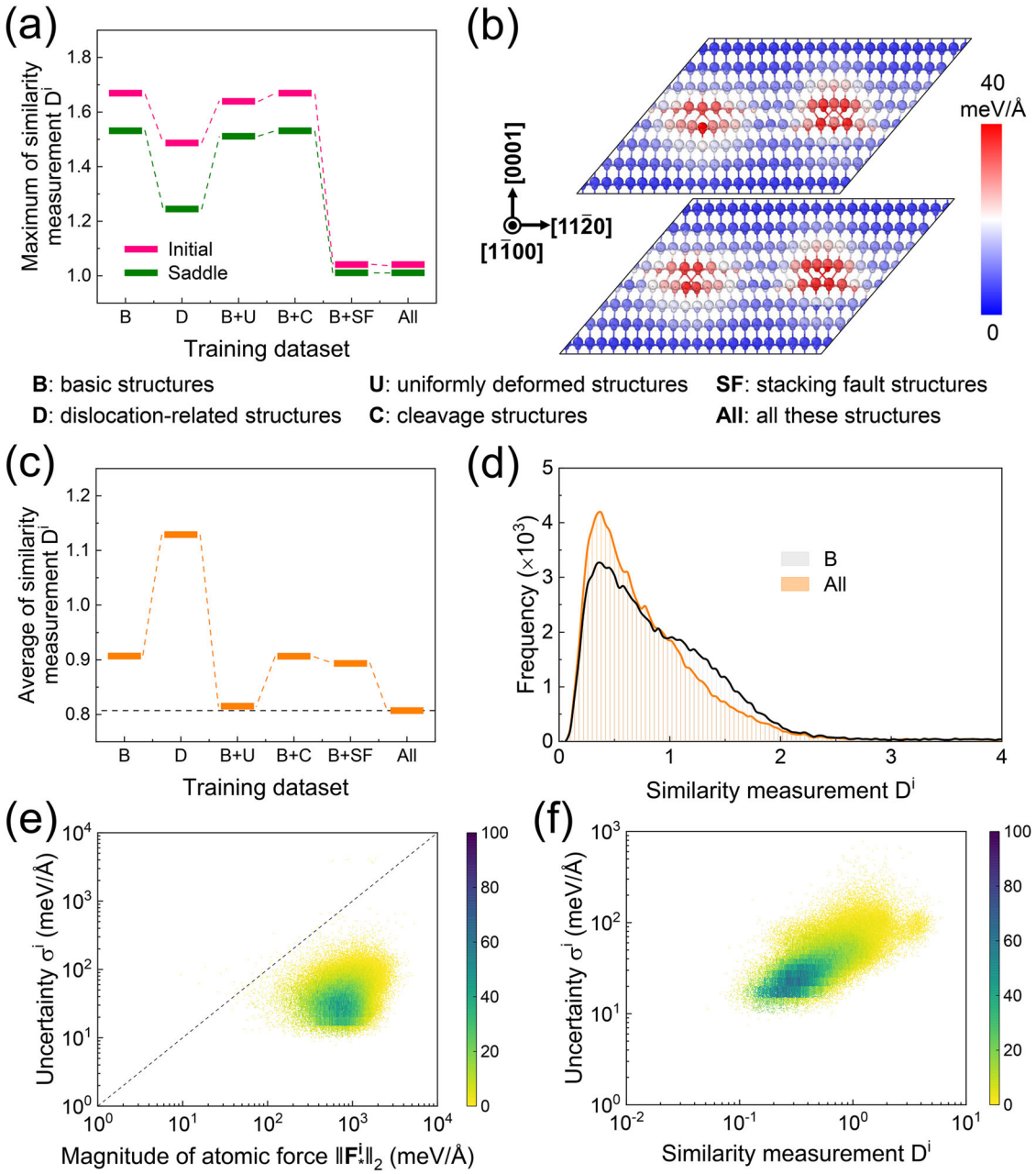

Fig. 13 | Atomic environment similarity and atomic force uncertainty. **a** Maximum value of similarity measurement D^i, i.e., $\max_i\{D^i\}$, in the dipole model of basal shuffle-set $1/3\langle 11\bar{2}0\rangle$ edge dislocation in reference to different sets of structures within the training dataset. **b** The dipole models, color-coded by the uncertainty σ^i, were relaxed by DFT at (Upper) initial and (Lower) saddle configuration as the dislocation slipped along [11$\bar{2}$0] directions. **c**–**f** Similarity and uncertainty for atoms in the snapshot shown in Fig. 12d, where only the results of the atoms within the defected structures are used. **c** Average value and **d** distribution of D^i with reference to different sets of structures within the training dataset. The scatter plot of the σ^i with **e** the magnitude of atomic force $\left\|\boldsymbol{F}_*^i\right\|_2$ and **f** the D^i. $\boldsymbol{F}_*^i$ represents the atomic force vector predicted by the NNP used to perform the nanoindentation simulation. Points in the graph are color-coded as value frequencies in each bin. Bin sizes are **e** [5,5] and **f** [0.0030,5].

associated with dislocation slip:

$$E_{\mathrm{P}} = \max_x\{E_{\mathrm{disl}}(x)\} - \min_x\{E_{\mathrm{disl}}(x)\}$$
$$\tau_{\mathrm{P}} = \max_x\left\{\frac{1}{b}\frac{\partial E_{\mathrm{disl}}(x)}{\partial x}\right\} \quad (2)$$

where b is the magnitude of the Burgers vector $\boldsymbol{b}$ of dislocation. Additionally, we investigated the effect of the cell geometry (i.e., the values of m and n) on the Peierls potential.

Nanopillar compression simulation

A c-oriented GaN nanopillar model with a diameter of 29 nm and a length of 53 nm was prepared, consisting of ~2.3 million atoms (see Fig. 11a, b). The models are periodic along the [0001] direction. The model was relaxed using the NPT ensemble at a temperature of 300 K and a timestep of 0.001 ps for 50 ps to release the stress along the [0001] direction. Subsequently, a uniaxial compressive load was applied by linearly rescaling the system length in the [0001] direction at a constant strain rate of 5×10^7 s^{-1} in an NVT ensemble at 300 K.

Nanoindentation simulation

An atomistic slab model of wurtzite ZnO, measuring 30.0 nm × 30.0 nm × 30.0 nm and consisting of ~2.1 million atoms, was constructed. The orientation of the model was set as x: $[1\bar{1}00]$, y: $[11\bar{2}0]$, and z: [0001] (see Fig. 12a). Before the nanoindentation simulations, the model was relaxed in an NPT ensemble at a temperature of 5 K and a timestep of 0.001 ps for 50 ps to release the in-plane stresses. To perform the displacement-controlled nanoindentation simulation, the z position of the spherical indenter with a radius R_{ind} = 10 nm was controlled to move along the z-axis at a speed of 5.0 m s^{-1} at a temperature of 5 K.

The repulsive force between the indenter and the slab model was assumed as follows:

$$F(r_{\text{ind}}) = \begin{cases} -\Lambda(r_{\text{ind}} - R_{\text{ind}})^2 & r_{\text{ind}} \le R_{\text{ind}} \\ 0 & r_{\text{ind}} > R_{\text{ind}} \end{cases} \tag{3}$$

where r_{ind} represents the distance of the atoms in the slab model to the centroid of the spherical indenter tip; Λ denotes a force constant related to the effective stiffness of the indenter[106,107], which was typically on the order of several eV · Å^{-3} and was set to 1.0 eV Å^{-3} in this work. A nanoindentation simulation with Λ = 10.0 eV Å^{-3} was also performed, and the results are identical to those of Λ = 1.0 eV Å^{-3}. During the indentation simulation, the center of mass of the atomic slab model was fixed, and the x and y dimensions of the slab model were relaxed such that the normal stress was 0 Pa in these directions.

Similarity measurement

The similarity of the atom i in the simulation snapshot to the training dataset is quantified as the minimum "distance" D^i of atom i from any atom j in the training dataset[108]:

$$D^i = \min_j \| \boldsymbol{G}_i^{\text{sim}} - \boldsymbol{G}_j^{\text{dataset}} \|_2 \tag{4}$$

where $\boldsymbol{G}$ is a fixed-size vector of atoms to describe their local environment up to the cutoff radius r_{cut}[20,109]; $\boldsymbol{G}_i^{\text{sim}}$ and $\boldsymbol{G}_j^{\text{dataset}}$ are the $\boldsymbol{G}$ vectors of the atom i in the simulation snapshot and the atom j in the training dataset, respectively. A smaller value of D^i indicates a greater similarity. In terms of the distances r_{ij} and r_{ik} of the atom i from its neighbors j and k and the angle subtended by those distances θ_{ijk}, the radial and angular components of $\boldsymbol{G}$ are given by:

$$\begin{aligned} G_i^{\text{rad}} &= \sum_{j \ne i} e^{-\eta(r_{ij} - r_s)^2} f(r_{ij}) \\ G_i^{\text{ang}} &= 2^{1-\zeta} \sum_{j,k \ne i} [1 + \cos(\theta_{ijk} - \theta_s)]^{\zeta} e^{-\eta[\frac{1}{2}(r_{ij} + r_{ik}) - r_s]^2} f(r_{ij}) f(r_{ik}) \end{aligned} \tag{5}$$

where the smooth cutoff function f is given by

$$f(r_{ij}) = \begin{cases} \frac{1}{2}\left[\cos\left(\frac{\pi r_{ij}}{r_{\text{cut}}}\right) + 1\right] & r_{ij} \le r_{\text{cut}} \\ 0 & r_{ij} > r_{\text{cut}} \end{cases} \tag{6}$$

and η, ζ, r_s, and θ_s are parameters, different for the radial and angular components. The vector $\boldsymbol{G}$ consists of multiple G_i^{rad} and G_i^{ang} elements, each of which is generated by varying the parameters η, ζ, r_s, and θ_s. Table S1 in the Supplementary Materials shows all values of there parameters selected in this study. The cutoff values r_{cut} are the same as those in NNP, i.e., 7.0 Å for ZnO and GaN, and 6.0 Å for $SrTiO_3$.

Uncertainty quantification

Ensemble-based models are among the most widely used and reliable methods for uncertainty quantification[53–56]. As proposed in ref. 53, ensemble-based methods surpass single deterministic models in terms of generalization and robustness, including methods like mean-variance estimation, deep evidential regression, and Gaussian mixture models. An ensemble involves training multiple neural networks using various sources of randomness during the training process, such as different initializations, stochastic optimization, or hyperparameter choices. Uncertainty is estimated by the variance of predictions from these NNPs within the ensemble, with greater prediction variation indicating higher uncertainty.

In the present work, we utilized ensemble-based models. Ten distinct NNPs were trained, which were independently initialized using different random seeds, influencing both the parameter initialization and the random selection of the testing dataset (which is 20% of the entire dataset). Since forces are derivatives of energy, they tend to display higher variability when overfitting occurs or when predictions are made outside the training domain. Therefore, forces are more suitable descriptors of epistemic uncertainty compared to energy-derived measures. For atom i in a system, the mth NNP in the ensemble, which consists of a total of M NNPs (M = 10 in this work), predicts the atomic forces $\boldsymbol{F}_m^i$. The uncertainty estimates σ^i for atom i are provided by the variances of the predicted atomic forces, which can be computed as

$$\sigma^i = \sqrt{\frac{1}{M}\sum_{m=1}^{M} \left\| \boldsymbol{F}_m^i - \hat{\boldsymbol{F}}^i \right\|_2^2} \tag{7}$$

where $\hat{\boldsymbol{F}}^i$ is the arithmetic mean of the predictions from each NNP in the ensemble, i.e., $\hat{\boldsymbol{F}}^i = \frac{1}{M}\sum_{m=1}^{M} \boldsymbol{F}_m^i$.

Data availability

All the training datasets and potential files used and/or constructed during the current study are available from the corresponding author on reasonable request.

Code availability

The code ADAIS to generate the dislocation-related structures via high-throughput DFT calculation as the training dataset is open-source. The source code and execution examples are available in our published article (see ref. 45).

Received: 19 July 2024; Accepted: 25 October 2024;
Published online: 22 November 2024

References

1. Nakamura, A., Matsunaga, K., Tohma, J., Yamamoto, T. & Ikuhara, Y. Conducting nanowires in insulating ceramics. *Nat. Mater.* **2**, 453–456 (2003).
2. Shibata, N. et al. Nonstoichiometric dislocation cores in α-alumina. *Science* **316**, 82–85 (2007).
3. Ikuhara, Y. Nanowire design by dislocation technology. *Prog. Mater. Sci.* **54**, 770–791 (2009).
4. Fang, X., Nakamura, A. & Rödel, J. Deform to perform: dislocation-tuned properties of ceramics. *Am. Cer. Soc. Bull.* **102**, 24–29 (2023).
5. Reddy, K. M. et al. Dislocation-mediated shear amorphization in boron carbide. *Sci. Adv.* **7**, eabc6714 (2021).
6. Oshima, Y., Nakamura, A. & Matsunaga, K. Extraordinary plasticity of an inorganic semiconductor in darkness. *Science* **360**, 772–774 (2018).
7. Sun, B. et al. Dislocation-induced thermal transport anisotropy in single-crystal group-iii nitride films. *Nat. Mater.* **18**, 136–140 (2019).
8. Höfling, M. et al. Control of polarization in bulk ferroelectrics by mechanical dislocation imprint. *Science* **372**, 961–964 (2021).
9. Zhuo, F. et al. Anisotropic dislocation-domain wall interactions in ferroelectrics. *Nat. Commun.* **13**, 6676 (2022).
10. Kissel, M. et al. Enhanced photoconductivity at dislocations in $SrTiO_3$. *Adv. Mater.* **34**, 2203032 (2022).

11. Gao, P. et al. Atomic-scale structure relaxation, chemistry and charge distribution of dislocation cores in $SrTiO_3$. *Ultramicroscopy* **184**, 217–224 (2018).
12. Salamania, J. et al. Elucidating dislocation core structures in titanium nitride through high-resolution imaging and atomistic simulations. *Mater. Des.* **224**, 111327 (2022).
13. Kondo, S., Mitsuma, T., Shibata, N. & Ikuhara, Y. Direct observation of individual dislocation interaction processes with grain boundaries. *Sci. Adv.* **2**, e1501926 (2016).
14. Lewis, G. & Catlow, C. Potential models for ionic oxides. *J. Phys. C Solid State Phys.* **18**, 1149 (1985).
15. Stillinger, F. H. & Weber, T. A. Computer simulation of local order in condensed phases of silicon. *Phys. Rev. B* **31**, 5262 (1985).
16. Vashishta, P., Kalia, R. K., Nakano, A. & Rino, J. P. Interaction potential for silicon carbide: a molecular dynamics study of elastic constants and vibrational density of states for crystalline and amorphous silicon carbide. *J. Appl. Phys*. **101**, 103515 (2007).
17. Van Duin, A. C., Dasgupta, S., Lorant, F. & Goddard, W. A. Reaxff: a reactive force field for hydrocarbons. *J. Phys. Chem. A* **105**, 9396–9409 (2001).
18. Shan, T.-R. et al. Charge-optimized many-body potential for the hafnium/hafnium oxide system. *Phys. Rev. B* **81**, 125328 (2010).
19. Salles, N., Politano, O., Amzallag, E. & Tétot, R. Molecular dynamics study of high-pressure alumina polymorphs with a tight-binding variable-charge model. *Comput. Mater. Sci.* **111**, 181–189 (2016).
20. Behler, J. & Parrinello, M. Generalized neural-network representation of high-dimensional potential-energy surfaces. *Phys. Rev. Lett.* **98**, 146401 (2007).
21. Behler, J. Four generations of high-dimensional neural network potentials. *Chem. Rev.* **121**, 10037–10072 (2021).
22. Artrith, N. & Urban, A. An implementation of artificial neural-network potentials for atomistic materials simulations: Performance for tio2. *Comput. Mater. Sci.* **114**, 135–150 (2016).
23. Artrith, N., Morawietz, T. & Behler, J. High-dimensional neural-network potentials for multicomponent systems: applications to zinc oxide. *Phys. Rev. B* **83**, 153101 (2011).
24. Miyagawa, T., Mori, K., Kato, N. & Yonezu, A. Development of neural network potential for md simulation and its application to tin. *Comput. Mater. Sci.* **206**, 111303 (2022).
25. Selvaratnam, B., Koodali, R. T. & Miró, P. Prediction of optoelectronic properties of cu2o using neural network potential. *Phys. Chem. Chem. Phys.* **22**, 14910–14917 (2020).
26. Thong, H.-C. et al. Machine learning interatomic potential for molecular dynamics simulation of the ferroelectric knbo3 perovskite. *Phys. Rev. B* **107**, 014101 (2023).
27. Shimizu, K. et al. Using neural network potentials to study defect formation and phonon properties of nitrogen vacancies with multiple charge states in gan. *Phys. Rev. B* **106**, 054108 (2022).
28. He, R. et al. Structural phase transitions in $SrTiO_3$ from deep potential molecular dynamics. *Phys. Rev. B* **105**, 064104 (2022).
29. Wu, J., Zhang, Y., Zhang, L. & Liu, S. Deep learning of accurate force field of ferroelectric Hfo_2. *Phys. Rev. B* **103**, 024108 (2021).
30. Wen, T. et al. Specialising neural network potentials for accurate properties and application to the mechanical response of titanium. *npj Comput. Mater.* **7**, 206 (2021).
31. Kobayashi, R., Giofré, D., Junge, T., Ceriotti, M. & Curtin, W. A. Neural network potential for al-mg-si alloys. *Phys. Rev. Mater.* **1**, 053604 (2017).
32. Mori, H. & Ozaki, T. Neural network atomic potential to investigate the dislocation dynamics in bcc iron. *Phys. Rev. Mater.* **4**, 040601 (2020).
33. Stricker, M., Yin, B., Mak, E. & Curtin, W. Machine learning for metallurgy ii. a neural-network potential for magnesium. *Phys. Rev. Mater.* **4**, 103602 (2020).
34. Whitworth, R. Charged dislocations in ionic crystals. *Adv. Phys.* **24**, 203–304 (1975).
35. Vandermause, J. et al. On-the-fly active learning of interpretable bayesian force fields for atomistic rare events. *npj Comput. Mater.* **6**, 20 (2020).
36. Zhang, Y. et al. Dp-gen: a concurrent learning platform for the generation of reliable deep learning based potential energy models. *Comput. Phys. Commun.* **253**, 107206 (2020).
37. Zaverkin, V. et al. Uncertainty-biased molecular dynamics for learning uniformly accurate interatomic potentials. *npj Comput. Mater.* **10**, 83 (2024).
38. Kim, M., Seo, J.-H., Singisetti, U. & Ma, Z. Recent advances in free-standing single crystalline wide band-gap semiconductors and their applications: GaN, SiC, ZnO, β-Ga_2O_3, and diamond. *J. Mater. Chem. C.* **5**, 8338–8354 (2017).
39. Yang, Z. et al. Epitaxial $SrTiO_3$ films with dielectric constants exceeding 25,000. *Proc. Natl Acad. Sci. USA* **119**, e2202189119 (2022).
40. Lymperakis, L., Neugebauer, J., Albrecht, M., Remmele, T. & Strunk, H. Strain induced deep electronic states around threading dislocations in gan. *Phys. Rev. Lett.* **93**, 196401 (2004).
41. Porz, L. et al. Conceptual framework for dislocation-modified conductivity in oxide ceramics deconvoluting mesoscopic structure, core, and space charge exemplified for $SrTiO_3$. *ACS Nano* **15**, 9355–9367 (2020).
42. Ohno, Y. et al. Optical properties of dislocations in wurtzite ZnO single crystals introduced at elevated temperatures. *J. Appl. Phys.* **104**, 073515 (2008).
43. Sun, C. et al. Resilient ZnO nanowires in an irradiation environment: an in situ study. *Acta Mater.* **95**, 156–163 (2015).
44. Marrocchelli, D., Sun, L. & Yildiz, B. Dislocations in $SrTiO_3$: easy to reduce but not so fast for oxygen transport. *J. Am. Chem. Soc.* **137**, 4735–4748 (2015).
45. Zhang, S. H., Fu, Z. H. & Zhang, R. F. Adais: automatic derivation of anisotropic ideal strength via high-throughput first-principles computations. *Comput. Phys. Commun.* **238**, 244–253 (2019).
46. Kresse, G. & Furthmüller, J. Efficient iterative schemes for ab initio total-energy calculations using a plane-wave basis set. *Phys. Rev. B* **54**, 11169 (1996).
47. Zhang, R. F. et al. First-principles design of strong solids: approaches and applications. *Phys. Rep.* **826**, 1–49 (2019).
48. Ogata, S., Li, J. & Yip, S. Ideal pure shear strength of aluminum and copper. *Science* **298**, 807–811 (2002).
49. Ohno, Y. et al. Slip systems in wurtzite ZnO activated by vickers indentation on $\{21^{-}1^{-}0\}$ and $\{101^{-}0\}$ surfaces at elevated temperatures. *J. Cryst. Growth* **393**, 119–122 (2014).
50. Bradby, J. et al. Contact-induced defect propagation in ZnO. *Appl. Phys. Lett.* **80**, 4537–4539 (2002).
51. Basu, S. & Barsoum, M. W. Deformation micromechanisms of ZnO single crystals as determined from spherical nanoindentation stress–strain curves. *J. Mater. Res.* **22**, 2470–2477 (2007).
52. Jin, L., Guo, X. & Jia, C. TEM study of 〈110〉-type 35.26° dislocations specially induced by polishing of $SrTiO_3$ single crystals. *Ultramicroscopy* **134**, 77–85 (2013).
53. Tan, A. R., Urata, S., Goldman, S., Dietschreit, J. C. & Gómez-Bombarelli, R. Single-model uncertainty quantification in neural network potentials does not consistently outperform model ensembles. *npj Comput. Mater.* **9**, 225 (2023).
54. Jeong, W., Yoo, D., Lee, K., Jung, J. & Han, S. Efficient atomic-resolution uncertainty estimation for neural network potentials using a replica ensemble. *J. Phys. Chem. Lett.* **11**, 6090–6096 (2020).
55. Zhu, A., Batzner, S., Musaelian, A. & Kozinsky, B. Fast uncertainty estimates in deep learning interatomic potentials. *J. Chem. Phys*. **158**, 164111 (2023).

56. Kahle, L. & Zipoli, F. Quality of uncertainty estimates from neural network potential ensembles. *Phys. Rev. E* **105**, 015311 (2022).
57. Dezerald, L. et al. Ab initio modeling of the two-dimensional energy landscape of screw dislocations in bcc transition metals. *Phys. Rev. B* **89**, 024104 (2014).
58. Cai, W., Bulatob, V. V., Chang, J., Li, J. & Yip, S. Periodic image effects in dislocation modelling. *Philos. Mag.* **83**, 539–567 (2003).
59. Ventelon, L., Willaime, F., Clouet, E. & Rodney, D. Ab initio investigation of the peierls potential of screw dislocations in bcc fe and w. *Acta Mater.* **61**, 3973–3985 (2013).
60. Clouet, E., Ventelon, L. & Willaime, F. Dislocation core field. ii. screw dislocation in iron. *Phys. Rev. B* **84**, 224107 (2011).
61. Vitek, V. Intrinsic stacking faults in body-centred cubic crystals. *Philos. Mag.* **18**, 773–786 (1968).
62. Schoeck, G. The generalized peierls–nabarro model. *Philos. Mag. A* **69**, 1085–1095 (1994).
63. Erhart, P. et al. Analytic bond-order potential for atomistic simulations of zinc oxide. *J. Phys. Condens. Matter* **18**, 6585 (2006).
64. Agrawal, R., Peng, B., Gdoutos, E. E. & Espinosa, H. D. Elasticity size effects in ZnO nanowires- a combined experimental-computational approach. *Nano Lett.* **8**, 3668–3674 (2008).
65. Thomas, B., Marks, N. & Begg, B. Developing pair potentials for simulating radiation damage in complex oxides. *Nucl. Instrum. Methods Phys. Res. B Beam Interact. Mater. At.* **228**, 288–292 (2005).
66. Furushima, Y., Arakawa, Y., Nakamura, A., Tochigi, E. & Matsunaga, K. Nonstoichiometric [012] dislocation in strontium titanate. *Acta Mater.* **135**, 103–111 (2017).
67. Henkelman, G., Arnaldsson, A. & Jónsson, H. A fast and robust algorithm for bader decomposition of charge density. *Comput. Mater. Sci.* **36**, 354–360 (2006).
68. Ewald, P. P. Die berechnung optischer und elektrostatischer gitterpotentiale. *Ann. der Phys.* **369**, 253–287 (1921).
69. Ko, T. W., Finkler, J. A., Goedecker, S. & Behler, J. A fourth-generation high-dimensional neural network potential with accurate electrostatics including non-local charge transfer. *Nat. Commun.* **12**, 398 (2021).
70. Hockney, R. W. & Eastwood, J. W. *Computer Simulation Using Particles* (CRC Press, 2021).
71. Jia, C., Thust, A. & Urban, K. Atomic-scale analysis of the oxygen configuration at a $SrTiO_3$ dislocation core. *Phys. Rev. Lett.* **95**, 225506 (2005).
72. Hirth, J. P. & Lothe, J. *Theory of Dislocations* (Krieger Publishing, 1982).
73. Magagnosc, D. J., Derenge, M. A. & Jones, K. A. First formed dislocations in microcompressed c-oriented gan micropillars and their subsequent interactions. *J. Appl. Phys*. **128**, 045107 (2020).
74. Huang, J. et al. Dislocation cross-slip in gan single crystals under nanoindentation. *Appl. Phys. Lett.* **98**, 221906 (2011).
75. Krimsky, E. et al. Nano-indentation used to study pyramidal slip in gan single crystals. *J. Appl. Phys.* **123**, 065701 (2018).
76. Oguri, H. et al. Bringing the photoplastic effect in ZnO to light: A photoindentation study on pyramidal slip. *J. Eur. Ceram. Soc.* **44**, 1301–1305 (2024).
77. Wang, H., Zhang, L., Han, J. & Weinan, E. Deepmd-kit: a deep learning package for many-body potential energy representation and molecular dynamics. *Comput. Phys. Commun.* **228**, 178–184 (2018).
78. Lu, D. et al. 86 pflops deep potential molecular dynamics simulation of 100 million atoms with ab initio accuracy. *Comput. Phys. Commun.* **259**, 107624 (2021).
79. Öezgüer, Ü. et al. A comprehensive review of ZnO materials and devices. *J. Appl. Phys*. **98**, 041301 (2005).
80. Pandey, R., Jaffe, J. E. & Harrison, N. M. Ab initio study of high pressure phase transition in gan. *J. Phys. Chem. Solids* **55**, 1357–1361 (1994).
81. Martin, G., Strite, S., Thornton, J. & Morkoc, H. Electrical properties of gaas/gan/gaas semiconductor-insulator-semiconductor structures. *Appl. Phys. Lett.* **58**, 2375–2377 (1991).
82. Li, Y. et al. Phase transitions and domain structures in strained pseudocubic (100) $SrTiO_3$ thin films. *Phys. Rev. B* **73**, 184112 (2006).
83. Hachemi, A., Hachemi, H., Ferhat-Hamida, A. & Louail, L. Elasticity of $SrTiO_3$ perovskite under high pressure in cubic, tetragonal and orthorhombic phases. *Phys. Scr.* **82**, 025602 (2010).
84. Kresse, G. & Joubert, D. From ultrasoft pseudopotentials to the projector augmented-wave method. *Phys. Rev. B* **59**, 1758 (1999).
85. Perdew, J. P., Burke, K. & Ernzerhof, M. Generalized gradient approximation made simple. *Phys. Rev. Lett.* **77**, 3865 (1996).
86. Perdew, J. P. et al. Restoring the density-gradient expansion for exchange in solids and surfaces. *Phys. Rev. Lett.* **100**, 136406 (2008).
87. Methfessel, M. P. A. T. & Paxton, A. T. High-precision sampling for brillouin-zone integration in metals. *Phys. Rev. B* **40**, 3616 (1989).
88. Monkhorst, H. J. & Pack, J. D. Special points for brillouin-zone integrations. *Phys. Rev. B* **13**, 5188 (1976).
89. van de Walle, A. & Ceder, G. Automating first-principles phase diagram calculations. *J. Phase Equilibria* **23**, 348–359 (2002).
90. Zhang, S. H. & Zhang, R. F. Aelas: Automatic elastic property derivations via high-throughput first-principles computation. *Comput. Phys. Commun.* **220**, 403–416 (2017).
91. Hill, R. The elastic behaviour of a crystalline aggregate. *Proc. Phys. Soc. Sect. A* **65**, 349 (1952).
92. Hill, R. Elastic properties of reinforced solids: some theoretical principles. *J. Mech. Phys. Solids* **11**, 357–372 (1963).
93. Plimpton, S. Fast parallel algorithms for short-range molecular dynamics. *J. Comput. Phys.* **117**, 1–19 (1995).
94. Maras, E., Trushin, O., Stukowski, A., Ala-Nissila, T. & Jonsson, H. Global transition path search for dislocation formation in ge on si (001). *Comput. Phys. Commun.* **205**, 13–21 (2016).
95. Stukowski, A. & Albe, K. Extracting dislocations and non-dislocation crystal defects from atomistic simulation data. *Model. Simul. Mater. Sci. Eng.* **18**, 085001 (2010).
96. Stukowski, A. Visualization and analysis of atomistic simulation data with ovito–the open visualization tool. *Model. Simul. Mater. Sci. Eng.* **18**, 015012 (2009).
97. Carreras, A. Phonolammps. https://phonolammps.readthedocs.io/en/master/index.html (2019).
98. Togo, A. & Tanaka, I. First principles phonon calculations in materials science. *Scr. Mater.* **108**, 1–5 (2015).
99. Bulatov, V. & Cai, W. *Computer Simulations of Dislocations* (Oxford Univ. Press, 2006).
100. Rodney, D., Ventelon, L., Clouet, E., Pizzagalli, L. & Willaime, F. Ab initio modeling of dislocation core properties in metals and semiconductors. *Acta Mater.* **124**, 633–659 (2017).
101. Henkelman, G., Uberuaga, B. P. & Jónsson, H. A climbing image nudged elastic band method for finding saddle points and minimum energy paths. *J. Chem. Phys.* **113**, 9901–9904 (2000).
102. Henkelman, G. & Jónsson, H. Improved tangent estimate in the nudged elastic band method for finding minimum energy paths and saddle points. *J. Chem. Phys.* **113**, 9978–9985 (2000).
103. Jónsson, H., Mills, G. & Jacobsen, K. W. in *Classical and Quantum Dynamics in Condensed Phase Simulations* (eds Berne, B. J., Coker, D. F. & Ciccotti, G.) Ch. 16 (World Scientific, 1998).
104. Zhang, S. H., Legut, D. & Zhang, R. F. Pnadis: an automated peierls-nabarro analyzer for dislocation core structure and slip resistance. *Comput. Phys. Commun.* **240**, 60–73 (2019).
105. Joos, B. & Duesbery, M. The peierls stress of dislocations: an analytic formula. *Phys. Rev. Lett.* **78**, 266 (1997).
106. Kelchner, C. L., Plimpton, S. & Hamilton, J. Dislocation nucleation and defect structure during surface indentation. *Phys. Rev. B* **58**, 11085 (1998).

107. Lilleodden, E., Zimmerman, J., Foiles, S. & Nix, W. Atomistic simulations of elastic deformation and dislocation nucleation during nanoindentation. *J. Mech. Phys. Solids* **51**, 901–920 (2003).
108. Naghdi, A. D. et al. Neural network interatomic potentials for open surface nano-mechanics applications. *Acta Mater.* **277**, 120200 (2024).
109. Smith, J. S., Isayev, O. & Roitberg, A. E. Ani-1: an extensible neural network potential with dft accuracy at force field computational cost. *Chem. Sci.* **8**, 3192–3203 (2017).
110. Li, G. et al. Mechanical properties in thermoelectric oxides: ideal strength, deformation mechanism, and fracture toughness. *Acta Mater.* **149**, 341–349 (2018).
111. Janotti, A. & Van de Walle, C. G. Native point defects in ZnO. *Phys. Rev. B* **76**, 165202 (2007).
112. Lide, D. *CRC Handbook of Chemistry and Physics* 89th edn (Taylor & Francis, 2008).
113. Carlotti, G., Fioretto, D., Socino, G. & Verona, E. Brillouin scattering determination of the whole set of elastic constants of a single transparent film of hexagonal symmetry. *J. Phys. Condens. Matter* **7**, 9147 (1995).
114. Bateman, T. Elastic moduli of single-crystal zinc oxide. *J. Appl. Phys.* **33**, 3309–3312 (1962).
115. Soumelidou, M.-M. et al. Strain and elastic constants of gan and inn. *Comput. Condens. Matter* **10**, 25–30 (2017).
116. Schulz, H. & Thiemann, K. Crystal structure refinement of aln and gan. *Solid State Commun.* **23**, 815–819 (1977).
117. Gian, W., Skowronski, M. & Rohrer, G. S. Structural defects and their relationship to nucleation of gan thin films. *MRS Online Proc. Libr.* **423**, 475 (1996).
118. Polian, A., Grimsditch, M. & Grzegory, I. Elastic constants of gallium nitride. *J. Appl. Phys.* **79**, 3343–3344 (1996).
119. Piskunov, S., Heifets, E., Eglitis, R. & Borstel, G. Bulk properties and electronic structure of $SrTiO_3$, $BaTiO_3$, $PbTiO_3$ perovskites: an ab initio hf/dft study. *Comput. Mater. Sci.* **29**, 165–178 (2004).
120. Bell, R. & Rupprecht, G. Elastic constants of strontium titanate. *Phys. Rev.* **129**, 90 (1963).
121. Nord, J., Albe, K., Erhart, P. & Nordlund, K. Modelling of compound semiconductors: analytical bond-order potential for gallium, nitrogen and gallium nitride. *J. Phys. Condens. Matter* **15**, 5649 (2003).
122. Béré, A. & Serra, A. On the atomic structures, mobility and interactions of extended defects in gan: dislocations, tilt and twin boundaries. *Philos. Mag.* **86**, 2159–2192 (2006).

Acknowledgements

S.Z. and S.O. were supported by the JSPS Postdoctoral Fellowships for Research in Japan (Standard), the Grant-in-Aid for JSPS Research Fellow (Grant No. 22F22056), and the JSPS KAKENHI (Grant No. JP22KF-241), and were used computational resources of supercomputer Fugaku provided by the RIKEN Center for Computational Science (Project IDs: hp230205 and hp230212), the large-scale computer systems at the Cybermedia Center, Osaka University, and the Large-scale parallel computing server at the Center for Computational Materials Science, Institute for Materials Research, Tohoku University. S.O. acknowledges the support by the Ministry of Education, Culture, Sport, Science and Technology of Japan (Grant Nos. JPMXP1122684766, JPMXP1020230325, and JPMXP1020230327), and the support by JSPS KAKENHI (Grant Nos. JP23H00161 and JP23K20037). Y.L. and A.N acknowledge the support by the Japan Society for the Promotion of Science (JSPS) KAKENHI JP24H00285, JP24H00032, JP24K17169, and JP22K14143.

Author contributions

S.Z.: methodology, software, formal analysis, and original draft writing; Y.L. and A.N.: writing—review & editing; S.S.: methodology; S.O.: conceptualization, writing—review & editing, supervision, and project management. All authors contributed to discussions and the final manuscript.

Competing interests

The authors declare no competing interests.

Additional information

Supplementary information The online version contains supplementary material available at https://doi.org/10.1038/s41524-024-01456-7.

Correspondence and requests for materials should be addressed to Shigenobu Ogata.

Reprints and permissions information is available at http://www.nature.com/reprints

Publisher's note Springer Nature remains neutral with regard to jurisdictional claims in published maps and institutional affiliations.

Open Access This article is licensed under a Creative Commons Attribution 4.0 International License, which permits use, sharing, adaptation, distribution and reproduction in any medium or format, as long as you give appropriate credit to the original author(s) and the source, provide a link to the Creative Commons licence, and indicate if changes were made. The images or other third party material in this article are included in the article's Creative Commons licence, unless indicated otherwise in a credit line to the material. If material is not included in the article's Creative Commons licence and your intended use is not permitted by statutory regulation or exceeds the permitted use, you will need to obtain permission directly from the copyright holder. To view a copy of this licence, visit http://creativecommons.org/licenses/by/4.0/.

© The Author(s) 2024